Atomistic structure investigation of Eu–doped ZnO nano-sponges

Shihui Feng,[1,*] Sarmad Naim Katea,[2] Markus Ek,[2] Gunnar Westin,[2] Cheuk-Wai Tai,[1,*]

[1]Department of Material and Environmental Chemistry, Arrhenius laboratory, Stockholm University, SE 10691 Stockholm, Sweden
[2]Department of Chemistry-Ångström, Ångström Laboratory, Uppsala University, Uppsala, SE 75121, Sweden

*Correspondence: cheuk-wai.tai@mmk.su.se (C.T); shihui.feng@mmk.su.se (S.F)

Summary

ZnO is a semiconductor with a wide range of applications and often the properties are modified by metal-ion doping. The distribution of dopant atoms within the ZnO crystal strongly affects the optical and magnetic properties making it crucial to describe the structure down to the atomic level. This study reveals the dopant structure and contents in Eu-doped ZnO nano-phase sponges with up to 20% $EuO_{1.5}$. High-resolution STEM imaging, EELS and electron pair-distribution function (ePDF) provided atomic distances. The Eu was distributed over the ZnO:Eu crystals, but in addition, an amorphous inter-crystalline phase was observed, especially in the 20% Eu sample. The ePDF analysis revealed the presence of non-periodic Eu(III)-oxide clusters and that there were significant changes in Eu coordination between the samples, which is ascribed as due to the inter-crystalline phase. The proposed method offers a potential characterization routine for a detailed investigation of complex doped materials.

Keywords: Eu-doped ZnO; dopant-ion distribution; electron pair-distribution function.

Zinc oxide (ZnO) is a widely used abundant material of low toxicity showing a unique combination of properties including a wide bandgap (3.4 eV), high electron mobility, wide range of optical transparency, and room temperature luminescence.[1–3] These properties have led to many current applications and promises of application in as diverse fields as transparent electrodes[4], batteries[5], catalysis, photo-/electro-catalysis for water and gas remediation[6–8], solar-cells[9–13], and sensors.[14,15] Doping with different ions, in particular d- and f-block elements, can be used to modify the structural, optical, electrical, and magnetic properties. Therefore, much attention is paid to metal doping of ZnO, especially when considering utilization of optic and magnetic properties in multi-functional devices.[16,17] Many metal-ion dopants have sizes and coordination requirements making them unlikely to fit the ZnO host structure. Nevertheless, there are many reports of high doping levels with these ions. One of the most studied group of dopants is that of the large alio-valent Ln-ions[18] where there has been an ongoing debate on the viability and nature of the claims of doping levels of 5 at.% Ln and higher.[18] Another problem arising when trying to understand the effect of adding dopant ions is the often highly varying properties found with similar doping levels and even rather similar synthesis routes. These differences are likely the results of impurities, crystal quality differences, ion valence and local dopant coordination. This is a general problem that has hampered progress in many important research fields such as solar cells, solar-hydrogen catalysis, and diluted magnetic semiconductors (DMS).[19,20]

Many applications of ZnO depend on good electronic transport while retaining a large available surface area interacting with electrolytes or species to be chemically converted or sensed in gas or liquid phase. Nano-crystalline sponges combine intimate metal-oxide crystal interfaces while still possessing a large surface area. Moreover, nano-sponges may be produced from low-cost simple chemicals with extremely short heating times of a few minutes or less.[21] Also, for a rational design of doped semiconductor oxides, it is of great interest to investigate the nature of the dopants within the ZnO structures. In previous work, the much debated local dopant structure in Eu-doped ZnO nano-sponges with as much as 5 mol% of $EuO_{1.5}$ in ZnO was studied.[21,22] It was found that Eu-oxide-clusters were present within the ZnO structure without much disturbance and change in the size of the ZnO lattice.

Therefore, the possibility of increasing the Eu-oxide doping level, even beyond 5% was explored to find out how much of Eu-oxide clusters that can be accommodated within the ZnO structure and what happens when this dopant level is exceeded. X-ray diffraction (XRD) and IR spectroscopy indicated a change in doping mode between 10 and 20 at.% Eu. SEM, XRD, and IR spectroscopy, used here are techniques describing the average structure but do not provide information on the local structural changes on a very fine nano- or atomic-scale required to understand these complex materials. At these high doping levels, it is not unlikely that more than one kind of Eu-doped ZnO is present. Advanced HRTEM techniques were applied to examine the nano-crystalline ZnO:Eu sponges doped with 5 at.% and 20 at.% Eu at scales from entire sponge particles, via the ca. 10-20 nm sized ZnO:Eu crystals and grain-boundaries to atomic scale. HAADF-STEM imaging, of which the contrast strongly relies on the sample thickness and atomic number (Z), was used together with electron diffraction to reveal the structure at atomic scale. To gain a comprehensive understanding of the local atomic structure and correlations between europium, zinc, and oxygen atoms, as well as structural ordering and a possible secondary phase, electron pair-distribution-function (PDF) was used to reveal the atom-atom distances in a chosen area. PDF shows the probability of finding an atom at a certain distance r from a given atom. This function can be mathematically described as follows:

$$\boldsymbol{g(r) = \frac{1}{4\pi\rho_0 r^2 N}\sum_i\sum_{j\neq i}\delta(r-r_{ij})}$$

Where $\boldsymbol{N}$ is the total atom number in the system studied, $\boldsymbol{\rho_0}$ the average number density of atoms, $\boldsymbol{r_{ij}}$ the distance between atom $\boldsymbol{i}$ and atom $\boldsymbol{j}$, and $\boldsymbol{\delta(r-r_{ij})}$ the Dirac-delta function, which equals a single unit only when $\boldsymbol{r = r_{ij}}$. The above equation illustrates the meaning of PDF, while each atom-atom distance could not be directly measured in a real experiment. The reduced PDF (rPDF) was commonly used to describe the structure features. This correlation function can be written as:

$$\boldsymbol{G(r) = (\frac{2}{\pi})\int_{Q_{min}}^{Q_{max}} F(Q)\sin(Qr)\,dQ}$$

Where $\boldsymbol{Q}$ is the momentum transfer vector or the so-called wave vector, $\boldsymbol{F(Q)}$ is the reduced structure function, $\boldsymbol{Q_{max}}$ and $\boldsymbol{Q_{min}}$ are the maximum and minimum limitations of momentum transfer vector in the diffraction experiment, respectively. The $\boldsymbol{F(Q)}$ can be obtained by making structure function $\boldsymbol{S(Q)}$ independent to the wave vector in order to amplify the signal at high $\boldsymbol{Q}$ range. The advantages of using rPDF is that it can be directly derived from the scattering data which make random uncertainties constant, while getting PDF $\boldsymbol{g(r)}$ also needs an assumption of the value of the average number density, which is hard to obtain accurately by experiment. In addition to the atom-atom distance, both PDF and rPDF can provide information about structural features, including coordination number, average atom density, and atomic periodicity. During the last decades, PDF analysis was mainly based on X-ray and neutron scattering and became a well-established technique for the structural characterization of crystalline[23] and amorphous materials.[24,25] As for X-ray PDF and neutron PDF, electron-PDF was obtained by applying Fourier transformation to structure function-$\boldsymbol{S(Q)}$. Such a structure function can easily be extracted from electron diffraction patterns. Here, by utilizing the advantages of the high spatial resolution and tuneable illumination area given by TEM, the PDF profile could be obtained at micron-scale to small nano-scale.

Five samples with different the Eu doping the concentrations 0, 5, 10, 20, and 33 mol% $EuO_{1.5}$ in ZnO (given below as: 0Eu, 5Eu, 10Eu, 20Eu and 33Eu) heated at 600 and 650 °C for 3 minutes were investigated. From previous studies, it was found that 5Eu nano-sponges could be obtained at 200 °C, 3 min. These sponges showed XRD patterns completely assignable to *h*-ZnO with very minor changes in unit cell-parameters.[22] However, TEM, XPS, TGA and IR spectroscopy showed the presence of minor amounts of organic residues which were replaced by Eu-oxo-carbonate when heating at 300 – 500 °C for 3 minutes. Heating at 600 °C for 3 min. removed the carbonate and yielded a pure oxide 5Eu nano-crystalline sponge without detectable phase separation. Upon heating at 700 °C, TEM revealed a few emerging ca. 1-3 nm sized Eu_2O_3 crystals at the ZnO:Eu sponge surface which grew into nano-sized *c*-Eu_2O_3 at higher temperatures. With lower Eu loading, the phase separation occurred at higher temperatures of up to 900 °C. The Eu-oxide was found to be homogeneously distributed within the ca. 10 nm sized ZnO:Eu crystals building up the nano-sponges while the XRD unit cell-parameters were virtually unchanged. EXAFS and DFT modelling suggested that $(EuO_{1.5})_{4-8}$ clusters were present inside the ZnO crystals, in excellent agreement with the experimental data.[22] This surprising finding explained how large amount of Eu-ions can be incorporated into ZnO without much change of XRD unit cell-parameters. With such high Eu-loading there should only be less than ca. 2 nm of ZnO between the Eu-oxide clusters. The studies also indicated that the window of carbonate-free and non-phase-separated pure ZnO:Eu nano-sponges extends to even higher Eu-doping levels.

It was therefore interesting to investigate in detail how high Eu-doping levels the ZnO:Eu nano-sponges can be accommodated without phase separation detectable with XRD, and what structures form when exceeding the maximum Eu-doping limit. Herein, XRD and IR spectroscopy were used to find out the temperature limits for the presence of carbonate (lowest T) and phase separation (highest T) versus Eu-oxide concentration. Considering the doping model with 4 to 8 Eu membered non-periodic oxide clusters in crystalline *h*-ZnO given in literature,[22] it should only be possible to reach 10-15% $EuO_{1.5}$ in the ZnO before there is not enough ZnO to cover each cluster with one layer of ZnO. However, XRD and IR spectroscopy describe the materials as an average over the volume of the material which does not allow for obtaining important details on where the Eu resides, its oxidation state, the Zn- and Eu-to-oxygen coordination spheres, and the presence of more than one phase. Therefore, an extensive study using TEM/STEM in real-space and reciprocal-space was used to provide the detailed structural features of the ZnO:Eu nano-sponges. The STEM images and spectroscopy showed that the Eu was present in the ZnO crystals, but also formed an Eu(III)-oxide rich inter-crystalline amorphous phase, especially pronounced with the higher Eu-doping levels. The ePDF revealed atom-atom pair distances within the ZnO:Eu sponges, which further proved the existence of Eu-oxide within the ZnO as well as the Eu-rich inter-crystalline boundary phase.

Result and Discussion

Overall phase analysis of Eu-doped ZnO

Overall phase analysis of Eu-doped ZnO with 0, 5, 10, 20, and 33 mol% $EuO_{1.5}$ in ZnO (ZnO:0-33Eu) were made with powder-XRD and IR spectroscopy to investigate the metastable limit for carbonate-free Eu-oxide doping of ZnO without phase separation, i.e. with retained *h*-ZnO XRD patterns and Zn-O vibration peak in the IR spectra.

XRD patterns of 0, 5, 10, 20 and 33EuZnO sponges heated for 3 minutes at 600 and 650 °C, respectively, are shown in Figure 1. The corresponding unit cell-parameters are given in Table 1. It can be observed that the diffractograms obtained after heating sponges with compositions of up to 33Eu to 600 and 650 °C, respectively, were quite similar in showing *h*-ZnO:Eu as the only identifiable crystalline phase. Very broad and overlapping peaks at ~28.6 and ~29.7° 2θ came up stronger while the ZnO:Eu peaks were strongly reduced in intensity with increased Eu-loading. The broad peaks are associated to the non-periodic $[EuO_{1.5}]_n$ clusters. The 33Eu sample showed very weak *h*-ZnO peaks overlapping the broad peaks which prevented unit cell-parameters to be extracted. The unit cell-parameters of the Eu-doped *h*-ZnO:Eu phase were very similar for the two synthesis temperatures, differing in the *a/b*- and *c*-axis lengths only by < 0.003 Å, which is within the error of the determination for samples made with the same Eu-loading. The pure ZnO sample showed a larger difference in unit cell-parameters between the samples heated at 600 and 650 °C, which might be due to an easier relaxation of the lattice while removing defects when there are no Eu-oxide clusters present.

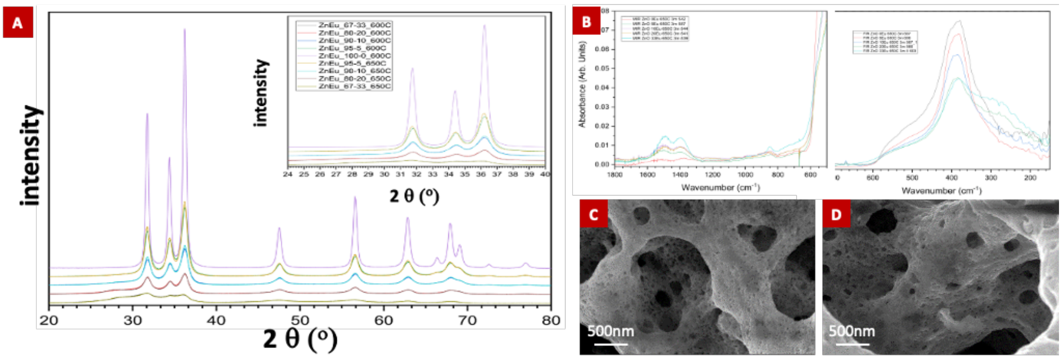

Figure 1. Overall phase analysis of ZnO: Eu

(A) XRD of 0, 5, 10, 20 and 33% $EuO_{1.5}$ in ZnO (ZnO:0-33Eu) heated at 600 and 650 °C for 3 min, respectively.

(B) IR spectra of ZnO:Eu nano-sponges with 0, 5, 10, 20 and 33% EuO1.5 in ZnO heated to 650 °C. (left) mid-IR range (1800-400 cm-1) and (right) far-IR range (700-180 cm-1).

(C, D) SEM images of ZnO:Eu nano-crystalline sponges heated to 650 °C. (C) 5Eu and (D) 20 Eu.

Table 1. Unit cell-parameters for *h*-ZnO:Eu.

ZnO:Eu (%Eu)	0	5	10	20
a (Å) 600 °C	3.25076 (8)	3.2518 (3)	3.2494 (6)	3.246 (1)
a (Å) 650 °C	3.2478 (1)	3.2515 (3)	3.2497 (6)	3.247 (1)
c (Å) 600 °C	5.2081 (1)	5.2054 (5)	5.202 (1)	5.196 (2)
c (Å) 650 °C	5.2027 (3)	5.2040 (4)	5.201 (1)	5.199 (2)
Vol. (Å^3) 600 °C	47.662 (3)	47.670 (1)	47.57 (2)	47.41 (4)
Vol. (Å^3) 650 °C	47.528 (4)	47.650 (1)	47.57 (2)	47.48 (4)

IR spectra obtained in the mid- and far-IR range of 0-33Eu nano-sponges heated at 650 °C are shown in Figure 1B left and right, respectively. The IR spectra of ZnO:0-20Eu nano-sponges heated at 600 °C were very similar to those obtained after heating at 650 °C indicating small differences in contents and structure. The 33Eu sample heated at 600 °C differed in the presence of weak multiplet bands around 1060 and 1240 cm^{-1} which were absent in the sample heated at 650 °C. All samples showed weak peaks at 1580-1300 cm^{-1}, assigned as due to symmetric and asymmetric C-O stretching in Eu-oxo-carbonate, along with water bending modes at 1640 cm^{-1}. The very weak peak at 840-860 cm^{-1} is also associated to the carbonate group. These water and carbonate peaks were quite weak compared to the main Zn-O vibration peak at ~390 cm^{-1}. The water and carbonate are likely formed by absorption H_2O and CO_2 from the atmosphere, although very minor amounts of internal Eu-oxo-carbonate remaining from the lower synthesis temperatures cannot be excluded. This applies especially to the 33Eu sample which showed somewhat more intense and differently shaped carbonate peaks, compared to the 0-20Eu samples. The Zn-O vibration band ranging from 600 to 300 cm^{-1} with a maximum at ca. 390 cm^{-1} was significantly reduced in intensity with increased Eu-content. In addition to the peak assigned to various Zn-O vibrations, a broad band was observed at 350-200 cm^{-1} which increased in relative intensity with Eu content, especially when comparing the 0-10Eu samples with the 20Eu and 33Eu samples. This band is assigned mainly to Eu-O vibrations in a non-crystalline state.

Thus, the XRD data indicated that as much as 33 mol% $EuO_{1.5}$ may be present without formation of other crystalline phases such as *c*-Eu_2O_3, even after heating at 650 °C. There was no strong trend in *h*-ZnO unit cell-parameters amongst the very similarly sized ZnO:Eu samples, although a very small reduction in unit cell-volume with increased Eu-content from 5 to 20% Eu was observed. The IR spectra gave similar results as the XRD patterns with the 0-10Eu samples showing similar Zn-O peaks and a very weak band associated to Eu-O vibrations, while the 20Eu and more so the 33Eu sample, showed a relatively stronger Eu-O vibration band. The 33Eu sample also stood out with a differently shaped carbonate peak band, compared to the lower Eu-loadings. This indicates that at least 10% Eu can be present as Eu-oxide clusters in the ZnO crystal in a similar fashion as described for the previously studied 5Eu sample,[22] while the 20Eu sample seem to have at least partially some other mode of Eu-doping, and the 33%Eu may have a substantial part of the Eu-oxide doping in a different way than found for the 5Eu sample.

The SEM images presented in Figure 1C and 1D show overall ZnO:Eu sponge micro-structures with a wide range of pore sizes from nm in the ZnO:Eu walls to µm between the walls. Thus, the structures were very similar for the 5Eu and the 20Eu sponges. No signs of phase separation were observed at this scale.

Atomic scale structure characterization

The XRD and IR studies indicated that the 10Eu sample had a similar doping mode as the 5Eu sample, while the 20-33Eu sponges showed differences indicating that a different doping mode was at least partially present. As mentioned above, from structural considerations, extending the $(EuO_{1.5})_{4-8}$ oxide cluster doping model previously obtained with EXAFS, XRD and DFT for the 5Eu samples[22] seem possible only to ca. 10-15% Eu with the higher concentration for the larger oxide clusters with eight Eu-atoms. At higher doping levels, there would not be enough ZnO to surround the Eu-oxide clusters. Therefore, a detailed study was conducted on the 20Eu sample to find out how the Eu is distributed in this sample. The 5Eu sample was studied for comparison after heating to 650 °C in similarity with the 20Eu sample. This is higher than 600 °C used in previous studies with up to 5 mol% $EuO_{1.5}$ and below 700 °C, which was previously shown to be the onset temperature for Eu_2O_3 crystallisation.[22]

HAADF-STEM was used to distinguish europium containing phases, where the large difference in atomic number for zinc (30) and europium (63) provide good contrast. Figure 2A-2C shows the overall morphology of ZnO:Eu sponges with 0 (pure ZnO), 5 and 20Eu compositions. The ZnO:Eu sponge structures are similar to those observed by SEM displaying varied pore sizes and ZnO:Eu sponge walls consisting of closely connected nano-crystals in sizes ranging from 6 to 8 nm. A difference between doped and non-doped sponges observed by STEM was that the doped samples (5Eu and 20Eu) had a higher degree of nano-porosity within the ZnO:Eu crystal-walls, in comparison with the non-doped ZnO. STEM-EDX mapping of the 5Eu sample (Figure 2d) and 20Eu (Figure 2e) showed the presence and distribution of oxygen (O), zinc (Zn), and europium (Eu). The EDX spectra and element compositions are provided in supplementary materials (Figure S1-S3).

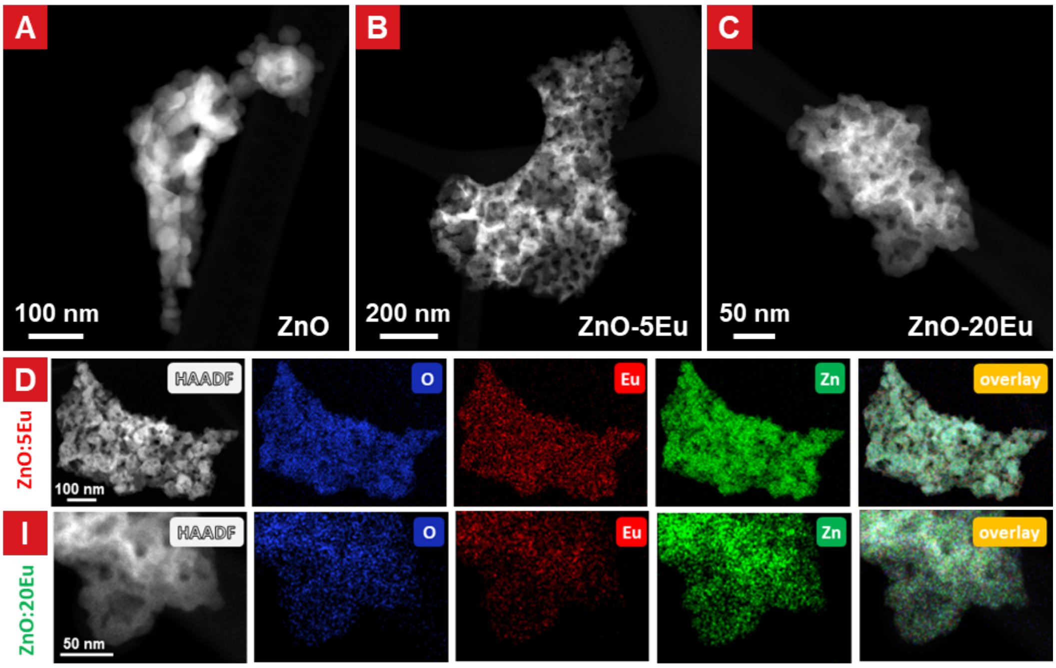

Figure 2. Morphology and Element mapping of ZnO:Eu nano-sponges

(A-C) HAADF-STEM images of ZnO (A), 5Eu (B), and 20Eu (C) samples showing the nano-sponge features. STEM-EDX mapping: 5Eu (D) and 20Eu (E) showing an even distribution of zinc, oxygen, and europium without obvious phase separation for both samples. Regional EDX spectra of doped samples, as well as EDX mapping of pure ZnO nano-sponges were provided in supplementary materials.

The detailed structural characterizations of the ZnO:Eu nano-sponges are presented in Figure 3. The magnified HAADF-STEM images showed brighter contrast between the ZnO:Eu nano-crystals in both samples, suggesting an Eu-richer region. The 20Eu sample exhibited more of the Eu-rich inter-granular regions which were also wider at typically 5-10 Å thick, compared to the 5Eu sample. STEM-EDX mapping (Figure 3B, 3G) further confirmed the increase in Eu concentration in these inter-crystalline regions. The STEM-EDX line profile (Figure 3H) gives the elemental concentration variation from the boundary towards the ZnO:Eu nano-crystal. It shows a discernible decrease in the Eu signal, accompanied by an increase in the Zn signal for the ZnO:Eu crystal, while the O concentration remains relatively stable. This provides evidence for a higher concentration of Eu at the grain boundaries of the ZnO:Eu nano-crystals. In the case of the 20Eu nano-sponge, the extracted spectrum from two distinct regions and subsequent calculation of the normalized composition yielded an approximate Eu concentration at the crystal boundaries of 13 at.% as compared to 3 at.% within the nano-crystals (Figure S4). A similar comparison for the 5Eu sample yielded analogous results to those obtained for the 20Eu sample (Figure S5) with the Eu concentration at the crystal boundaries and within ZnO:Eu crystal being approximately 6 at.% Eu and 2 at.% Eu, respectively.

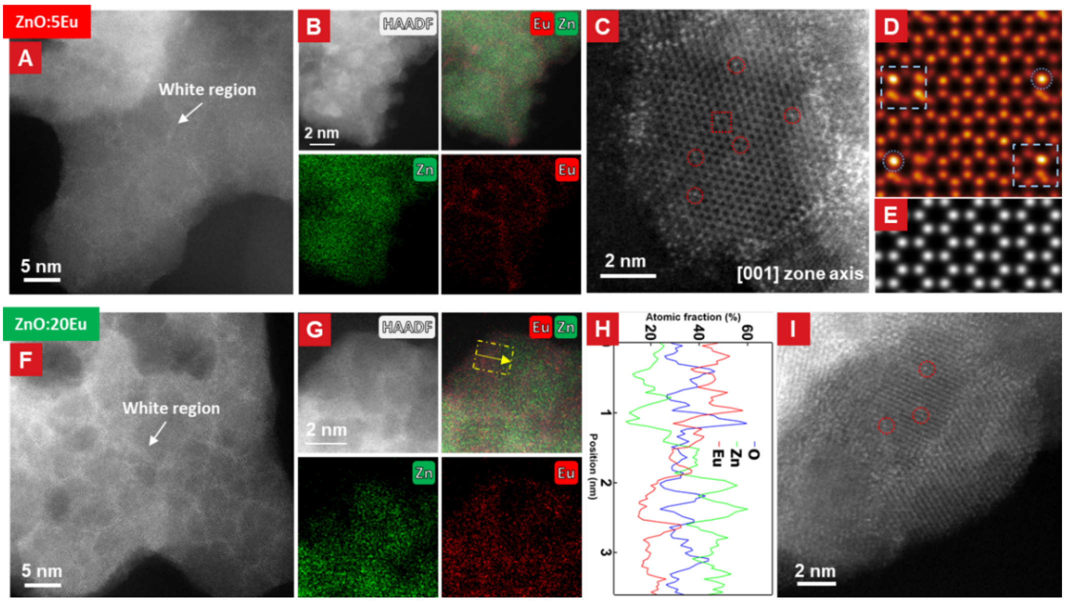

Figure 3. Structure characterization of ZnO:Eu samples

(A, F) HAADF-STEM images of 5Eu and 20Eu samples showing some bright-contrast regions in HAADF-STEM images indicating Eu-rich regions. (D, E) Simulated STEM-HAADF images of DFT calculated model with [001] zone axis. (B, G) High-resolution EDX shows an Eu-rich area between ZnO:Eu nano-crystals in the 5Eu and 20Eu samples. (H) STEM-EDX line profile extracted from G, showing the chemical variation between boundary and nano-crystal. (C, I) HRSTEM of two samples. The square mark in C indicates the area which has lattice distortion caused by Eu atoms. The circle mark in C, and H shows that the atom column contains Eu atoms with higher intensity.

Given the identification of Eu within the ZnO crystals and the observed segregation of Eu-oxide to the crystal boundaries, the distribution of Eu atoms within ZnO nano-crystals was investigated with atomic-resolution HAADF-STEM images (Figure 3C for 5Eu and Figure 3I for 20Eu). Some bright-contrast atomic columns were observed indicating the presence of dopant Eu atoms within the ZnO structure. To get a deeper understanding of the influence of Eu doping on HAADF contrast, simulated HAADF-STEM images were made by leveraging the doped structure[22] and the hexagonal ZnO structure along [001] zone axis. Certain brighter atomic columns in experimental data are marked by red circles in Figure 3C and 3I. Comparisons between the experimental data and simulated results, as well as our previous study, demonstrate a good fit. These images revealed that Eu doping in the ZnO structure lacks long-range periodicity, and instead exhibit a more random distribution. Moreover, it was found that the insertion of Eu atoms or clusters did not introduce significant lattice distortion into ZnO lattice which is line with the XRD data. The Eu cluster-like structure is labelled by a square mark in both the experimental and simulation data (Figure 3C and 3D). To ensure the representativeness of these findings, additional data were collected which are presented in the Supplementary Materials (Figure S6-S7).

Thus, the real space investigation confirmed the presence of Eu atoms within the ZnO nano-crystals. However, the model with 4-8 Eu atom sized oxide clusters present within the ZnO, as discussed in previous work for a 5Eu sample heated at 600 °C[22] was not unequivocally confirmed. The Eu-rich amorphous inter-crystalline phase revealed was most significant for the 20Eu sample, but was also present to some extent in the 5Eu sample. The rather homogenous thickness and nature of this ZnO:Eu grain-boundary phase showing 3-4 times higher relative Eu concentration than the ZnO:Eu crystals indicate that it was formed by expulsion of Eu-oxide from the highly Eu-doped metastable ZnO:Eu crystals during heat-treatment. The 20Eu sample is expected from a structural point of view to be able to include at most 10-15% Eu as 4 to 8 Eu atom sized clusters in the ZnO crystals, as there would not be enough ZnO to cover the clusters otherwise. The XRD and IR data indicated that the sample to have at least some material with a different doping mode besides that observed for the 5Eu and 10Eu sample. This difference might be connected to the Eu-rich ZnO:Eu crystal boundary phase observed mainly in the 20Eu sample, but also to some extent, in the 5Eu. The presence of this phase in the 5Eu sample may be due to the higher temperature used in this study compared to the previous one; 650 °C in the present study, compared to 600 °C in the previous study.[21,22] It was previously shown by TEM that the first very rare 2-3 nm sized Eu_2O_3 crystals formed at the ZnO:Eu sponge surface upon heating at 700 °C.[21,22] A more easy adaptation of the Eu-oxygen-coordination polyhedral and cluster is expected in the thin amorphous inter ZnO:Eu-crystal boundaries, not the least where ZnO:Eu crystals with misaligned lattice directions meet. For comparison, the 5-10 Å thickness in the 20Eu sample corresponds to ca. 2-4 Eu/ZnO_x units. The inter-crystalline phase may also include ZnO.

STEM-EELS was applied to explore the chemical properties of Eu. However, due to the broad peak of Zn *L*-edge and overlap between the Eu $M_{4,5}$ edge (1131 eV) and the Zn $L_{2,3}$ edge (1020 eV), only the background of the Zn pre-edge was employed for background subtraction. Figure 4A and 4B shows the elemental distribution of Zn and Eu. The Eu-rich region being much more pronounced for the 20Eu samples as revealed with HAADF-STEM and EDX was confirmed with the STEM-EELS mapping. The electron orbital occupancy can be calculated by analyzing the integrated intensity ratio between specific peaks in the EELS spectrum, thereby allowing for determination of the chemical valence states of selected elements and composition of the material. The signals in the EELS mapping were combined to get a high signal-noise ratio for chemical analysis. Figure 4C shows the summed EELS profiles of the 5Eu and 20Eu samples, respectively. Here the EELS spectrum was normalized using the integral intensity of Zn (ranging from 1020 – 1121 eV) and compared with the relative intensity of the Eu signal. In concert with EDX data, it was found that the Eu concentration in the 5Eu sample was not as high as for the 20Eu sample. The peak shape and the strong white-line features in both spectra, indicated that the europium was present as Eu-ions, rather than pure metal which should show weaker peaks around 1130 eV. From the literature, EuO and other Eu^{2+} compounds are unlikely to be present here as they are very susceptible to oxidation under the synthesis conditions used here.[26] Also, by comparing the relative intensity ratio between the Eu M_4 and M_5 edges, the valence state of europium could be set as +3, which is in accordance with the literature.[21,22,27]

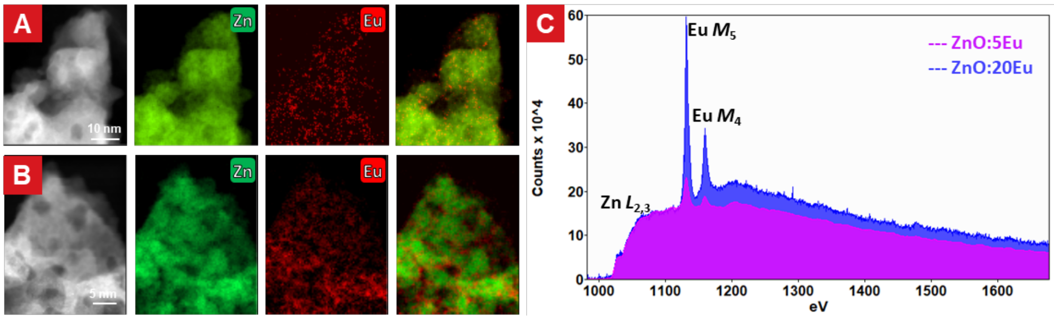

Figure 4. EELS-STEM analysis of 5Eu and 20Eu samples
(A, B) EELS mapping of Zn and Eu of 5Eu (A) and 20Eu (B).
(C) Summed EELS spectra from every scanning pixel in EELS map.

Electron pair-distribution function (ePDF) analysis

As discussed above, the distribution of Eu and Zn atoms in the 5Eu and 20Eu nano-sponges were obtained from micrometre to nanometre scale by the HAADF-STEM and EELS studies. To get a closer insight into the local atomic structure, the inter-atomic distances were investigated with ePDF. Figure 5A shows the calculated rPDF of a standard *h*-ZnO structure (PDF card 00-036-1451) and the experimental rPDF of the 5Eu and 20Eu samples.

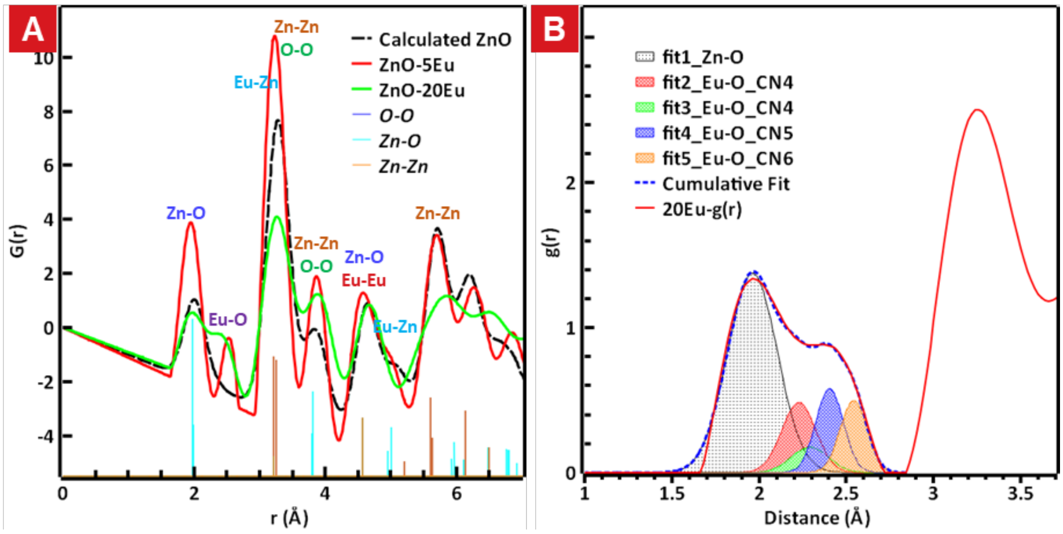

Figure 5. PDF profiles of calculated ZnO and experimental 5Eu and 20Eu data
(A) Reduced PDF profiles of calculated ZnO and experimental 5Eu and 20Eu.
(B)Deconvolution of peaks at *r* = 2.1-2.8 Å in 20Eu sample.

The most obvious differences between the 5Eu and 20 Eu samples and the *h*-ZnO rPDF were the peaks found at *r* = 2.1-2.8 Å, which were absent in the calculated *h*-ZnO rPDF. The peaks at longer distances showed significant variations between the samples, but as these peaks originate from several different atom-pairs having similar distances, these peaks were more difficult to analyse in detail. Tentative assignments of the atom-pairs contributing to the composite peaks in the range *r* = 1.5-5.5 Å was made based on the DFT generated theoretic structures with ZnO containing 4.1% Eu as Eu4 or Eu8 oxide clusters[22] and a calculated *h*-ZnO structure as follows: 1.9-2.1 Å (Zn-O), 2.1-2.8 Å (Eu-O), 3.0-3.7 Å (Eu-Zn, Zn-Zn, O-O, Eu-Zn, Eu-O, Eu-Eu), 3.7-4.2 Å (Eu-O, Eu-Eu, Zn-O, Eu-O), 4.2-4.7 Å (Zn-Zn, O-O, Zn-O, Eu-Eu, Eu-Zn), 4.7-5.3 Å (Shoulder) (Eu-Zn, Zn-O, O-O), and 5.2-5-8 Å (Zn-Zn, O-O, Eu-Zn, Eu-Eu).

The ZnO:Eu samples and calculated *h*-ZnO *r*PDF showed a clear Zn-O peak at 1.97 Å (5Eu) – 2.02 Å (20Eu), which was overlapped by the broad Eu-O peak in the latter case. This peak fits the Zn-O distances given as 1.974-1.989 Å for *h*-ZnO (PDF card: 00-036-1451) well. The Zn^{2+}-ions of the *h*-ZnO are all tetrahedral four-coordinated by oxygen ions and the Zn-O distances also match the sum of the ionic radii of CN4 Zn^{2+}-and O^{2-}ions (60 + 140 pm).[28] A clear difference between the two ZnO:Eu samples could be observed in the Eu-O peaks. The 5Eu sample showed a single Eu-O peak at 2.2 – 2.7 Å, with a maximum at 2.51 Å. These Eu-O distances are in fair agreement with those obtained in the theoretic 4.1Eu structures containing oxide clusters with 4 or 8 Eu atoms.[22] The Eu-oxide clusters contain Eu^{3+}-ions coordinated mainly by 5 or 6 oxygen atoms, but in some cases a four-coordinated Eu-ion is present. This led to very unusual low average Eu CN:s of 5.2-5.5 for the theoretic structures fitting the experimental data quite well and yielding the lowest energy.[22] The 20Eu sample showed a much wider Eu-O peak covering distances from ca. 2.1 to 2.8 Å, with the peak shape at the longest distances of the band being similar to that of the 5Eu sample and a maximum at 2.40 Å. This broad band could tentatively be deconvoluted into serval peaks corresponding to different Eu-O coordination environments obtained from the modelled 4.1Eu structures (Figure 5B). The shortest Eu-O distances at ca. 2.1-2.4 Å fit the 2.22-2.26 Å found for four-coordinated Eu-ions in the theoretic Eu-oxide clusters[22], as well as the extrapolated sum of four-coordinated Eu-ions (0.84 Å)[21] and oxygen-ions (1.40 Å)[28] of 2.24 Å. The peak component at 2.3-2.5 Å, was supplemented by smaller component at 2.1-2.6 Å, to fit the rPDF of the 20Eu in this region. These two combined peak components are in good agreement with the 2.12-2.45 Å obtained for five-coordinated theoretic clusters in 4.1Eu structures, as well as the bond distance of 2.29 Å obtained from the extrapolated ionic radii of five-coordinated Eu^{3+}-ions (0.89 Å) and O^{2-}ions (140 pm).[21] The longest Eu-O bonds were in the range 2.4-2.6 Å, which is in line with the ca. 2.50 Å obtained from the six-coordinated Eu^{3+}-ions in the theoretical 4.1Eu structures. This yields an Eu^{3+} ionic radius of 1.10 Å, which is longer than the reported experimentally obtained ionic radius of the Eu-ion (0.94 Å). The difference in ionic radii found for six-coordinated Eu-ions in the literature and the present and previously obtained experimental and theoretic structures may stem from the former being close packed crystalline structures while the latter are part of non-periodic Eu-oxide clusters containing differently coordinated Eu-ions adapting their coordination sphere to fit the ZnO lattice which show very little change due to the dopant clusters.

It showed that the 20Eu sample contain a broad range of Eu-ion coordination modes with a significantly increased fraction of Eu-ions in the very low four- and five-coordination to oxygen, compared to the 5Eu sample which clusters were dominated by five- and six-coordinated Eu-ions, yielding typical average Eu CN of 5.2-5.5.[22] However, it cannot be ruled out that there might also be higher coordinated Zn^{2+}-ions present, which based on the reported ionic radii of Zn^{2+} (0.88 Å) and O^{2-} (1.40 Å)[28] could have Zn-O bond distances of up to 2.28 Å for the six-coordinated Zn^{2+}-ions. This distance would overlap with the shortest distances for the four-coordinated Eu^{3+}-ions. Thus, the ePDF for the 5Eu sample gave results in good agreement with the previously obtained theoretical 4.1Eu structures with 4 or 8 Eu atom oxide clusters occupying space in the *h*-ZnO crystal with nearly no effect on its unit cell-dimensions. Interestingly, it was found that the 20Eu sample, while being similar to the 5Eu sample for the longer Eu-O bond-lengths, showed a substantial increase in Eu-ions coordinated to the very low four and five oxygen. However, the atom-atom distances of the four-coordinated Eu-ions overlap those of five- and six-coordinated Zn-ions and therefore it cannot be ruled out that the 20Eu sample also contained some higher Zn-ions coordination numbers than present in ZnO.

As the STEM-HAADF and EELS mapping showed, this sample contained a substantial amount of Eu-rich inter-crystalline amorphous phase. The theoretic 4.1Eu structures reported imply that a maximum of 10-15% $EuO_{1.5}$ clusters can be present in the *h*-ZnO while providing enough ZnO to cover the clusters with one layer of ZnO_4 tetrahedra. The ca. 5-10 Å (1-2 ZnO unit cells) thick amorphous inter-crystalline phase, to surround most ZnO:Eu crystals, could contain mainly low coordination Eu-ions and possibly some Zn-ions in higher five or six-coordinations, besides possible four-coordinated Zn-ions. The latter CN4 Zn^{2+}-ions would not be possible to distinguish those in the *h*-ZnO structure. The constraints of the ZnO crystal facets may affect the bonding between the crystalline and amorphous phases and the various ionic radii of the metal ions involved are likely best satisfied by an amorphous Zn-Eu-oxide structure. The Zn^{2+}- and Eu^{3+}-ions having spherical d^{10} and s^2 outer orbital shells without requirements of bond directions may make mixed coordination numbers and wide bond-length distributions facilitated. The different typical ionic sizes may be equalized in an amorphous structure by attaining the very low CN4 for Eu^{3+}-ions (84 pm) and CN 5/6 for Zn^{2+}-ions (74 pm/ 88 pm) which may allow for a tighter mixing of the ions. It can be mentioned that when looking at DFT generated Eu2 clusters in ZnO containing four- and five-coordinated Eu-ions, the mismatch in size of the Eu-ions and the surrounding crystalline ZnO structure caused a much larger increase in ZnO:Eu unit cell-dimensions associated with an increase in energy. This compared to the larger Eu-oxide clusters which more easily could adjust coordination within the larger cluster occupied cavity and thereby give very low increase in ZnO:Eu unit cell parameters and result in the lowest energies. In the amorphous structure described above there would not necessarily be a strain between the single Eu-ions or oxide clusters and ZnO as with the crystalline ZnO and therefore the formation energy may be lower compared to the crystalline case.

Nevertheless, the full PDF ($g(r)$) were also obtained based on applying proper average number density (ρ_0) (Figure S11). The calculated number density for 5Eu and 20Eu were 0.915 ± $5.5x10^{-7}$ and 1.11 ± $7.6x10^{-7}$ $Å^{-3}$, respectively. Hence, the coordination number was given in Table S1. Unfortunately, the calculated coordination number showed significant differences from EXAFS data from previous work, which indicates the inaccuracy of intensity even though no strong texture features were shown in diffraction patterns. The characteristics of TEM only allowed us to get information in a projection view from the sample, which may lead to smaller coordination number. In addition to the atom-atom distance, both PDF and rPDF can provide structural features, including coordination number, average atom density, and atom arrangement periodicity. In this context, the provided reduced PDF adequately described the structural characteristics of Europium in nanosponges and exhibiting a high precision in the average number density. However, the full PDF results diverge slightly from the experimental data obtained through EXAFS result in literature. This variance underscores the need for meticulous consideration in the calculation of the full PDF.

Conclusion

In this work, the structural features in ZnO:Eu nano-sponges were investigated from micrometre to atomic scale using STEM imaging, spectroscopy, and ePDF, as well as XRD and IR spectroscopy. It was found that at least 10% $EuO_{1.5}$ could be introduced into the *h*-ZnO with virtually no change in the structure compared to the 5Eu structure judging from the IR and XRD patterns, while addition of 20% $EuO_{1.5}$ led to significant formation of an amorphous, 5-10 Å thick Eu-rich inter-crystalline phase, besides the Eu-oxide dispersed as clusters in the ZnO:Eu crystals similar to the 5% $EuO_{1.5}$ sample studied. The inter-crystalline phase found by HAADF, EDX and EELS mapping, and the latter technique showed that Eu was trivalent in similarity with the Eu(III) in the ZnO:Eu crystals, which is in line with previous studies on 5% Eu samples. The ePDF was applied to get quantitative information on structural deviations on Eu-doping in different samples. The PDF peak intensities provided Eu-O and Eu-Eu distances which for the higher doped 20Eu sample showed peaks at 2.0 Å and 3.2 Å is lower than that of in 5Eu, indicates low possibility to find Zn-O and Zn-Zn atom pair at certain distance. Also, the broadened peak of 20Eu showed the there was more relatively lattice distortion and defects in this sample. The ePDF results are compatible well with all other experimental result above and fit the findings in previous studies. Moreover, the ePDF not only provided information how structure deviated from standard sample, as was acquired from STEM, but also gave precise atom-atom bonding information. The combination of imaging, spectroscopy and ePDF provided a rather unique in-depth spatial understanding of the details of structural variations that arise due to different doping levels. This combination of techniques provide a powerful tool for in-depth materials characterization including crystalline and amorphous phases of complex compositions in sizes down to less than a nanometre, thereby adding information not extractable from standard techniques.

EXPERIMENTAL PROCEDURES

Resource Availability

Lead Contact

Further information and requests for resources and reagents should be directed to and will be fulfilled by the Lead Contact, Cheuk-Wai Tai (cheuk-wai.tai@mmk.su.se).

Data and Code Availability

The data that support the plots within this paper, and other finding of this study, are available from the corresponding authors upon reasonable request.

Material synthesis

Nano-sponges synthesis.

Zinc diacetate tetrahydrate ($Zn(OAc)_2{*}4H_2O$), zinc dinitrate hexahydrate ($Zn(NO_3)_2{*}6H_2O$), triethanolamine (TEA), and Methanol (p.a.) were used as received. The synthesis of precursor pastes with 0, 5, 10, 20 and 33 mol% $EuO_{1.5}$ in ZnO was made as previously described for synthesis of ZnO:Eu pasts with up to 5 mol% $EuO_{1.5}$[21]. Shortly, zinc nitrate and acetate salts dissolved in methanol are complexed with 0.5 TEA per Zn and mixed. Then, the solution was evaporated until a clear or whitish paste is obtained. In the present study, the heat-treatment differed slightly from previous studies; instead of heating the paste directly at temperatures of 200 °C or higher for three minutes, it was firstly heated at 400 °C for 1 min, and thereafter to 600 or 650 °C for 3 min. When comparing microstructures and XRD patterns no significant difference was observed between the two techniques.

Characterization

X-ray diffraction.

Powder X-ray diffraction (XRD) patterns were obtained with a Bruker D8 equipped with a Lynxeye XE-T detector and using Cu Kα radiation (1.5460 Å) in θ-2θ mode over the range 10-100° 2θ. Determination of unit cell-dimensions of the h-ZnO was achieved with the Topas software version 6 applying the PDF card 00-036-1451 file from PDF-4+ as ZnO.

IR spectroscopy.

IR spectra were obtained in the Mid- (4000-370 cm^{-1}) and Far-IR (1000-150 cm^{-1}) ranges using a nitrogen purged Perkin-Elmer spectrum one instrument equipped with KBr and Polyethylene beam-splitters, for the Mid- and Far-IR range, respectively. The spectra were obtained with resolution of 2 cm-1 for the mid-IR range and 4 cm-1 for the far-IR range. The powder samples were studied on a diamond-ATR (Pike GladiATR) unit.

(S)TEM sample preparation.

The powder samples were dispersed in ethanol and subjected to ultrasonic treatment for 1 minute. The dispersion was then dripped onto a lacey carbon copper grid. The grid was dried using infrared light for 5 minutes. Then, the sample was placed in a plasma cleaner (Fischione Instruments model 1020) for 15 seconds to remove organic surface contamination.

(S)TEM experiment.

TEM data collection was performed using a double aberration-corrected Themis Z microscope (Thermofisher Scientific Inc) equipped with SuperXG2 EDX system. The aberration was corrected to 5th order. The experiments were carried out at 300 kV accelerating voltage, including TEM, STEM, and spectroscopy work. The convergence angle of STEM high-angle annular dark field imaging (STEM-HAADF) was set to 21 mrad with a probe current of 80 pA, while the inner and outer collection angles for the HAADF-STEM detector were selected as 64 and 200 mrad, respectively. To enhance the signal-to-noise ratio, the probe current was adjusted to 150 pA during the STEM energy dispersive X-ray (STEM-EDX) experiment. The EDX experiment were performed using 1024 x 1024 scan size to maintain the spatial resolution by 4 µs dwelling time. The atomic fraction maps were selected to present the EDX mapping. For the chemical analysis of europium and zinc, electron energy-loss spectroscopy (EELS) was applied. The EELS data were collected in STEM mode using the Gatan Quantum GIF with a 29.5 mm camera length with 5 mm entrance aperture and a collection semi-angle of 28.24 mrad. The low-loss and high-loss spectra were captured simultaneously in dual-EELS mode. The SNR mode ([1,130]x detector binning) was used for STEM-EELS to get a high signal-noise ratio data. Exposure time for each scanning pixel is 0.05 s with spatial drift correction every 5 rows. The electron diffraction patterns for the PDF study were acquired in TEM diffraction mode using the Oneview camera. To achieve a high q-range (resolution ring = 0.357 Å) while preserving the diffraction features, the camera length was set to 460 mm, and the exposure time for each diffraction pattern was 2 seconds.

Data processing and PDF simulation

The low-pass filter was applied to HAADF-STEM images to remove the high-frequency noise. The electron pair-distribution function can be calculated from the scattering profile. The Difftools[29], a Digitalmicrograph plugin package, was used to extract the scattering profile. SUePDF software[30] was used for ePDF calculation, the average number density ($\boldsymbol{\rho_0}$) were obtained by calculate the slope between first physical peak and origin. Hence, the full PDF ($g(r)$) can be obtained by following equation:

$$g(r) = \frac{G(r)}{4\pi r \rho_0} + \gamma(r)$$

Where $\gamma(r)$ is nanoparticle form factor which depending on the shape of the scatters. Considering the closely connected ZnO nanoparticles within our nanosponges, the form factor was simply set to 1 (bulk) in our case. Meanwhile, the coordination number (N_c) can be calculated by following equation:

$$N_c = \int_{r2}^{r1} 4\pi r^2 \rho_0 g(r) dr$$

The STEM image simulation was done by Dr.Probe software[31]. All image simulation parameters corresponded to the STEM data collection. The inner and outer collection angle of the HAADF-STEM detector was 64-200 mrad. The sample thickness was 8 nm, which equals the average particle size of ZnO nano-sponges. The EELS data processing were done by Digitalmicrograph, the standard and Hatree-Slater model was used to build the scattering crocs-section for Zn and Eu, respectively. The PDF simulation was carried out by the Debye PDF method in the Diffpy-CMI package[32] on the Eu8 structure.

SUPPLEMENTAL INFORMATION

The online version contains supplementary material available at xxxxx

Acknowledgement

This work was performed at the Electron Microscopy Centre, supported by the Department of Materials and Environmental Chemistry and Faculty of Science at Stockholm University, Sweden. Financial support by Swedish Research Council (grant no.: 2018-05260) is acknowledged. G.W., M.E. and S.N.K. gratefully acknowledge financial support from the O. E. Nycander foundation.

Author contribution

SH.F., CW.T. and G.W. initiated the discussion and designed the experiment. SH.F conducted the TEM/STEM experiment and analysis. S.N.K., M.E. and G.W. conducted the nano-sponge synthesis, XRD and IR experiments and analyses. All authors designed the paper and were involved in the analysis and discussion of the results. SH.F wrote the manuscript with contribution of all authors.

Competing Interest

The authors declare no competing interests.

References

1. Özgür, Ü., Alivov, Y.I., Liu, C., Teke, A., Reshchikov, M.A., Doğan, S., Avrutin, V., Cho, S.J., and Morkọ, H. (2005). A comprehensive review of ZnO materials and devices. J. Appl. Phys. *98*, 1–103. 10.1063/1.1992666.
2. Kharisov, B.I., Kharissova, O. V., García, B.O., Méndez, Y.P., and De La Fuente, I.G. (2015). State of the art of nanoforest structures and their applications. RSC Adv. *5*, 105507–105523. 10.1039/c5ra22738k.
3. Cauda, V., Pugliese, D., Garino, N., Sacco, A., Bianco, S., Bella, F., Lamberti, A., and Gerbaldi, C. (2014). Multi-functional energy conversion and storage electrodes using flower-like Zinc oxide nanostructures. Energy *65*, 639–646. 10.1016/j.energy.2013.12.025.
4. Nguyen, V.H., Resende, J., Papanastasiou, D.T., Fontanals, N., Jiménez, C., Muñoz-Rojas, D., and Bellet, D. (2019). Low-cost fabrication of flexible transparent electrodes based on Al doped ZnO and silver nanowire nanocomposites: Impact of the network density. Nanoscale *11*, 12097–12107. 10.1039/c9nr02664a.
5. Zhang, J., Gu, P., Xu, J., Xue, H., and Pang, H. (2016). High performance of electrochemical lithium storage batteries: ZnO-based nanomaterials for lithium-ion and lithium-sulfur batteries. Nanoscale *8*, 18578–18595. 10.1039/c6nr07207k.
6. Surbhi, Chakraborty, I., and Pandey, A. (2023). A review article on application of ZnO-based nanocomposite materials in environmental remediation. Mater. Today Proc. 10.1016/j.matpr.2023.02.041.
7. Osajima, J.A., Sá, A.S., Feitosa, R.P., Furtini, M.B., Honorio, L.M.C., Fonseca, M.G., Trigueiro, P., Caregnato, P., Triboni, E.R., and Silva-Filho, E.C. (2023). Improved remediation of contaminated water using ZnO systems via chemical treatment: applications, implications and toxicological mitigation. Sustain. Water Resour. Manag. *9*, 1–16. 10.1007/s40899-023-00818-1.
8. Lee, K.M., Lai, C.W., Ngai, K.S., and Juan, J.C. (2016). Recent developments of zinc oxide based photocatalyst in water treatment technology: A review. Water Res. *88*, 428–448. 10.1016/j.watres.2015.09.045.
9. Ma, J., Lin, Z., Guo, X., Zhou, L., Su, J., Zhang, C., Yang, Z., Chang, J., Liu, S., and Hao, Y. (2019). Low-Temperature Solution-Processed ZnO Electron Transport Layer for Highly Efficient and Stable Planar Perovskite Solar Cells with Efficiency Over 20%. Sol. RRL *3*, 1–10. 10.1002/solr.201900096.
10. Son, D.Y., Im, J.H., Kim, H.S., and Park, N.G. (2014). 11% efficient perovskite solar cell based on ZnO nanorods: An effective charge collection system. J. Phys. Chem. C *118*, 16567–16573. 10.1021/jp412407j.
11. Huang, J., Yin, Z., and Zheng, Q. (2011). Applications of ZnO in organic and hybrid solar cells. Energy Environ. Sci. *4*, 3861–3877. 10.1039/c1ee01873f.
12. Law, M., Greene, L.E., Johnson, J.C., Saykally, R., and Yang, P. (2005). Nanowire dye-sensitized solar cells. Nat. Mater. *4*, 455–459. 10.1038/nmat1387.
13. Hosono, E., Fujihara, S., Honma, I., and Zhou, H. (2005). The fabrication of an upright-standing zinc oxide nanosheet for use in dye-sensitized solar cells. Adv. Mater. *17*, 2091–2094. 10.1002/adma.200500275.
14. Kang, Y., Yu, F., Zhang, L., Wang, W., Chen, L., and Li, Y. (2021). Review of ZnO-based nanomaterials in gas sensors. Solid State Ionics *360*, 115544. 10.1016/j.ssi.2020.115544.
15. Das, S.N., Kar, J.P., Choi, J.H., Lee, T., Moon, K.J., and Myoung, J.M. (2010). Fabrication and characterization of ZnO single nanowire-based hydrogen sensor. J. Phys. Chem. C *114*, 1689–1693. 10.1021/jp910515b.
16. Patel, M., Pataniya, P.M., Patel, V., Sumesh, C.K., and Late, D.J. (2020). Large area, broadband and highly sensitive photodetector based on ZnO-WS2/Si heterojunction. Sol. Energy *206*, 974–982. 10.1016/j.solener.2020.06.067.
17. Zhao, F., Lin, J., Lei, Z., Yi, Z., Qin, F., Zhang, J., Liu, L., Wu, X., Yang, W., and Wu, P. (2022). Realization of 18.97% theoretical efficiency of 0.9 μm thick c-Si/ZnO heterojunction ultrathin-film solar cells via surface plasmon resonance enhancement. Phys. Chem. Chem. Phys. *24*, 4871–4880. 10.1039/d1cp05119a.
18. Marin, R., and Jaque, D. (2021). Doping Lanthanide Ions in Colloidal Semiconductor Nanocrystals for Brighter Photoluminescence. Chem. Rev. *121*, 1425–1462. 10.1021/acs.chemrev.0c00692.
19. Jabbar, I., Zaman, Y., Althubeiti, K., Al Otaibi, S., Ishaque, M.Z., Rahman, N., Sohail, M., Khan, A., Ullah, A., Del Rosso, T., et al. (2022). Diluted magnetic semiconductor properties in TM doped ZnO nanoparticles. RSC Adv. *12*, 13456–13463. 10.1039/d2ra01210c.

20. Perdomo, C.P.F., Almeida, D.F., Cancellieri, I.C., Garcia, L.A., Cardoso, A.L.F., and Gunnewiek, R.F.K. (2023). Magnetic and electric behavior of spike- and petal-like nanoscaled Cu:ZnO superstructures diluted magnetic semiconductors. Mater. Chem. Phys. *307*, 128051. 10.1016/j.matchemphys.2023.128051.
21. Katea, S.N., Broqvist, P., Kullgren, J., Hemmer, E., and Westin, G. (2020). Fast, Low-Cost Synthesis of ZnO:Eu Nanosponges and the Nature of Ln Doping in ZnO. Inorg. Chem. *59*, 7584–7602. 10.1021/acs.inorgchem.0c00472.
22. Mukherjee, S., Katea, S.N., Rodrigues, E.M., Segre, C.U., Hemmer, E., Broqvist, P., Rensmo, H., and Westin, G. (2023). Entrapped Molecule-Like Europium-Oxide Clusters in Zinc Oxide with Nearly Unaffected Host Structure. Small *19*, 1–16. 10.1002/smll.202203331.
23. Yamada, H., Tominaka, S., Ohara, K., Liu, Z., Okubo, T., and Wakihara, T. (2019). Structural Evolution of Amorphous Precursors toward Crystalline Zeolites Visualized by an in Situ X-ray Pair Distribution Function Approach. J. Phys. Chem. C *123*, 28419–28426. 10.1021/acs.jpcc.9b07232.
24. Gaillac, R., Pullumbi, P., Beyer, K.A., Chapman, K., Keen, D.A., Bennett, T.D., and Coudert, F.X. (2017). Liquid metal–organic frameworks. Nat. Mater. *16*, 1149–1155. 10.1038/NMAT4998.
25. Hou, J., Ashling, C.W., Collins, S.M., Krajnc, A., Zhou, C., Longley, L., Johnstone, D.N., Chater, P.A., Li, S., Coulet, M.V., et al. (2019). Metal-organic framework crystal-glass composites. Nat. Commun. *10*, 1–10. 10.1038/s41467-019-10470-z.
26. Caspers, C., Müller, M., Gray, A.X., Kaiser, A.M., Gloskovskii, A., Fadley, C.S., Drube, W., and Schneider, C.M. (2011). Chemical stability of the magnetic oxide EuO directly on silicon observed by hard x-ray photoemission spectroscopy. Phys. Rev. B - Condens. Matter Mater. Phys. *84*, 1–7. 10.1103/PhysRevB.84.205217.
27. Mundy, J.A., Hodash, D., Melville, A., Held, R., Mairoser, T., Muller, D.A., Kourkoutis, L.F., Schmehl, A., and Schlom, D.G. (2014). Hetero-epitaxial EuO interfaces studied by analytic electron microscopy. Appl. Phys. Lett. *104*. 10.1063/1.4867161.
28. Shannon, R.D. (1976). Revised effective ionic radii and systematic studies of interatomic distances in halides and chalcogenides. Acta Crystallogr. Sect. A *32*, 751–767. 10.1107/S0567739476001551.
29. Mitchell, D.R.G. (2008). DiffTools: Electron diffraction software tools for DigitalMicrograph^{TM}. Microsc. Res. Tech. *71*, 588–593. 10.1002/jemt.20591.
30. Tran, D.T., Svensson, G., and Tai, C.W. (2017). SUePDF: A program to obtain quantitative pair distribution functions from electron diffraction data. J. Appl. Crystallogr. *50*, 304–312. 10.1107/S160057671601863X.
31. Barthel, J. (2018). Dr. Probe: A software for high-resolution STEM image simulation. Ultramicroscopy *193*, 1–11. 10.1016/j.ultramic.2018.06.003.
32. Juhás, P., Farrow, C.L., Yang, X., Knox, K.R., and Billinge, S.J.L. (2015). Complex modeling: A strategy and software program for combining multiple information sources to solve ill posed structure and nanostructure inverse problems. Acta Crystallogr. Sect. A Found. Adv. *71*, 562–568. 10.1107/S2053273315014473.